Chemical Science

EDGE ARTICLE

Check for updates

Shortwave infrared absorbing and fluorescent BODIPY J-aggregates for high-contrast *in vivo* imaging

Zhiyong Jiang, [ID] [ab] Xiangjun Ma,[a] Kaixuan Song,[a] Tianzhu Wang,[a] Mengxi Dong,[a] Hang Liu,[a] Hu Gao, [ID] [a] Xiaoqing Wang, [ID] *[a] Jing Zhao [ID] *[bc] and Zhipeng Liu [ID] *[a]

J-Aggregates hold significant promise for high-resolution shortwave infrared (SWIR) imaging, yet achieving robust SWIR absorption and emission simultaneously has been hindered by hypsochromic shifts in absorption and emission quenching caused by undesirable H- and random aggregation. To address this, we developed highly fluorescent BODIPY J-aggregates exhibiting absorption and emission spanning 1000–1600 nm. A key innovation was the implementation of a zig–zag molecular design, which effectively suppressed H-aggregation and minimized intermolecular interactions, thereby enabling anti-quenching SWIR emission. This design strategy was successfully translated into practical applications, yielding water-soluble nanoparticles capable of micron-resolution, multiplexed fluorescence, and photoacoustic *in vivo* imaging. This work establishes crucial design principles for creating highly efficient SWIR imaging agents.

Introduction

Fluorescence imaging in the shortwave infrared (SWIR, 1000–2500 nm) region presents significant potential for high-resolution *in vivo* imaging due to enhanced tissue penetration, low light absorption and reduced scattering compared to visible and near-infrared (NIR) light.[1–3] As a result, developing imaging agents with efficient SWIR absorption and fluorescence profiles is essential for advancing this field.

Small organic molecule-based SWIR imaging agents have gained significant attention due to their superior biocompatibility and tunability.[4–7] To achieve SWIR imaging capabilities, molecular engineering strategies, including enhancing the intramolecular charge transfer (ICT) effect and expanding the π-conjugation structure,[5,7] have been employed on classical chromophores such as cyanines,[8–10] benzothiadiazoles,[11–13] xanthenes,[2,14,15] and boron dipyrromethenes (BODIPYs).[16,17] However, most of these dyes exhibit absorption maxima in the NIR region, typically requiring excitation with an 808 nm laser. Only a limited number of cyanine and xanthene dyes possess both absorption and emission wavelengths within the SWIR window.[2,8,15,18,19] Theoretical models suggest that NIR excitation

wavelengths significantly diminish deep tissue penetration and imaging resolution compared to SWIR excitation.[1,3] While cyanine dyes can achieve absorption and emission wavelengths exceeding 1000 nm, their chemical- and photo-stability require further improvement.[20–22] Additionally, enhancing the ICT effect to bathochromically shift the excitation and emission wavelengths of cyanine and xanthene dyes into the SWIR region often leads to reduced quantum yields,[2] compromising high-resolution fluorescence imaging. Thus, a critical challenge remains in identifying design strategies for small organic molecule-based SWIR imaging agents that achieve both efficient absorption and emission within the SWIR window.

J-Aggregation, a classical molecular aggregation mode characterized by "head-to-tail" interactions and slipping aggregation of molecules in the excited state,[23–25] offers a promising strategy to address the challenges of SWIR imaging.[26,27] J-aggregates typically exhibit significant bathochromic-shifts in absorption and emission wavelengths, reduced Stokes shifts, and increased quantum yields (Φ_f) compared to their monomeric counterparts. The feasibility of this strategy was first demonstrated in studies of cyanines. For instance, Sletten and Zhang achieved stable J-aggregates of IR-140 in hollow mesoporous silica nanoparticles and FD-1080 in amphiphilic phospholipids, resulting in absorption maxima at 1038 nm and 1047 nm, respectively, and emission at 1360 nm and 1370 nm, respectively.[28,29] Recently, Zhao *et al.* systematically investigated the effects of substituents on the SWIR performance of Cy7 J-aggregates, enabling multiplexed fluorescence and photoacoustic imaging *in vivo*.[30]

[a]College of Materials Science and Engineering, College of Science, Co-Innovation Center of Efficient Processing and Utilization of Forest Resources, Nanjing Forestry University, Nanjing 210037, China. E-mail: xqwang@njfu.edu.cn; zpliu@njfu.edu.cn
[b]Chemistry and Biomedicine Innovation Center (ChemBIC), State Key Laboratory of Coordination Chemistry, School of Chemistry and Chemical Engineering, Nanjing University, Nanjing 210023, China. E-mail: jingzhao@nju.edu.cn
[c]NJU Xishan Institute of Applied Biotechnology, Wuxi 214000, China

Various BODIPY dyes have also been reported to achieve SWIR absorption or emission through J-aggregation. By increasing intermolecular electrostatic repulsion or hydrogen bonding effects, Liu and Xiong developed several SWIR-emitting BODIPY J-aggregates, demonstrating excellent *in vivo* imaging abilities.[31,32] Utilizing a vinyl-bridging strategy, Liu and Hao regulated the J-aggregation performance of BODIPY and aza-BODIPY dimers, obtaining SWIR-absorbing J-aggregates with superior biophotonic applications.[33,34] Despite these promising advances, the rational design of SWIR-type BODIPY J-aggregates remains challenging.

Firstly, the J-aggregation properties of these reported dyes often rely on random screening. Notably, to achieve SWIR absorption, the designed dye molecules typically possess larger conjugated structures compared to visible or NIR-emissive J-aggregating dyes. Such structures tend to aggregate through π–π stacking, leading to H-aggregates or random aggregates, complicating the control of J-aggregation.[25,35,36] There is a need for more controllable strategies to manage J-aggregation while avoiding interference from H-aggregation and other random aggregation modes. Secondly, constructing highly efficient J-aggregate luminescence remains a challenge. Strong intermolecular interactions, such as π–π stacking and intermolecular charge transfer, often lead to fluorescence quenching.[36] NIR dyes with large conjugated structures struggle to avoid these interactions during J-aggregation, resulting in reported J-aggregates that generally exhibit fluorescence quenching compared to their monomers.[33,34] This characteristic significantly reduces the signal-to-noise ratio during SWIR imaging, hindering high-resolution imaging abilities. Therefore, achieving efficient J-aggregation while avoiding fluorescence quenching from strong intermolecular interactions is another major challenge in this field.

To address these challenges, we demonstrate that a dimeric zigzag-type donor (D)–π–acceptor (A) molecular design strategy is promising for constructing efficient SWIR-absorbing and emitting J-aggregates. We designed a series of 1,4-bisvinylbenzene-bridged zigzag BODIPY dyes (**BVB-BDP$_{agg}$1–8**) and rationalized that moderate inter- and intramolecular CT coupling, coupled with hindered intermolecular interactions, are the two key factors for achieving J-aggregation-induced SWIR absorption and emission in these compounds. The resulting J-aggregates exhibit bathochromic-shifted absorption and emission spectra in the SWIR region, with a brightness of up to 2736 M^{-1} cm^{-1}, significantly surpassing the imaging contrast of commercial cyanine probes such as ICG (120 M^{-1} cm^{-1}) and IR1061 (1400 M^{-1} cm^{-1}).[5] Furthermore, we demonstrated the excellent multiplexed SWIR imaging potential of these J-aggregates through *in vivo* fluorescence and photoacoustic imaging experiments.

Results and discussions

Molecular design

Our previous research has demonstrated that zigzag type ethylene-bridged BODIPY dimers tend to form J-aggregates in their aggregation state.[33] Although the J-aggregates of the

BODIPY dimers showed a typical bathochromic-shifted in the J-band within SWIR region, their fluorescence is significantly quenched due to intense ICT and intermolecular π–π stacking effects. Based on these preliminary findings, we propose that rationally designed zigzag type BODIPY dimers that weaken both ICT and intermolecular interactions could yield J-aggregates with enhanced SWIR absorption and fluorescence. To prove our hypothesis, we selected our previously developed 1,4-bisvinylbenzene-bridged BODIPY dimer (BVB-BDP) scaffold, which has relative weak ICT characteristics compared to the ethylene bridged BODIPY dimer. This scaffold served as the basis for designing of desired BODIPY dimers,[16] designated as **BVB-BDP$_{agg}$1–8** (Fig. 1b and S1).

In these compounds, we integrated electron-withdrawing groups (–CF$_3$ and –COOMe) as well as electron-donating groups (*p*-methoxyphenyl, *p*-methoxystyl, *p*-dimethylaminophenyl and *p*-dimethylaminostyl) at the *meso*- and 5,5'-positions of the BODIPY core. This modification aims to tune the ICT effect of the monomer and modulate the intermolecular D–A couplings in the aggregation state. Furthermore, the bridge formed by the 1,4-bisvinylbenzene group at 3,3'-position of the BODIPY cores was equipped with two octyl groups on the phenyl ring. In contrast to our previously reported BVB-BPD dyes with polyether chains, the introduction of octyl groups allows the BODIPY dyes to possess both polar D–A structures and non-polar characteristics. Consequently, the incorporation of alkyl chains not only facilitates preferred molecular aggregation but also inhibits intermolecular interactions within the aggregates. The synthesis of these compounds are outlined in Scheme S1, and the chemical structures of **BVB-BDP$_{agg}$1–4** were determined by X-ray single-crystal diffraction (Fig. S2 and Table S1).

Photophysical properties in the diluted solution

We initially characterized the absorption and emission spectra of **BVB-BDP$_{agg}$1–8** in diluted dichloromethane solution (Table S2 and Fig. S3). **BVB-BDP$_{agg}$1–8** showed mainly two absorption bands in the NIR and red regions, characterized by intense molecular absorption coefficient (ε, 10^5 M^{-1} cm^{-1}), which can be assigned to the first (S$_0$ → S$_1$) and second (S$_0$ → S$_2$) electronic transitions, respectively. Compounds with identical electron-donating groups displayed nearly identical absorption bands, indicating that variations in the electron-withdrawing ability of the –COOMe and –CF$_3$ at the *meso*-position have a negligible impact on the ground-state electronic structure of these compounds. On the other hand, **BVB-BDP$_{agg}$5–8** exhibited a bathochromic-shift of approximately 50 nm in their absorption maximum (λ_{abs}) compared to **BVB-BDP$_{agg}$1–4**, suggesting the double bond conjugation between the BODIPY core and the phenyl rings facilitates more efficient π-conjugation effect than direct single-bond conjugation.

Furthermore, all compounds exhibited relatively weak and broad emission bands spanning 900 to 1300 nm, demonstrating their potential as single-molecular SWIR fluorophores. Although the broad emission band hindered detailed peak assignment, it is evident that **BVB-BDP$_{agg}$1–2** and **BVB-BDP$_{agg}$5–**
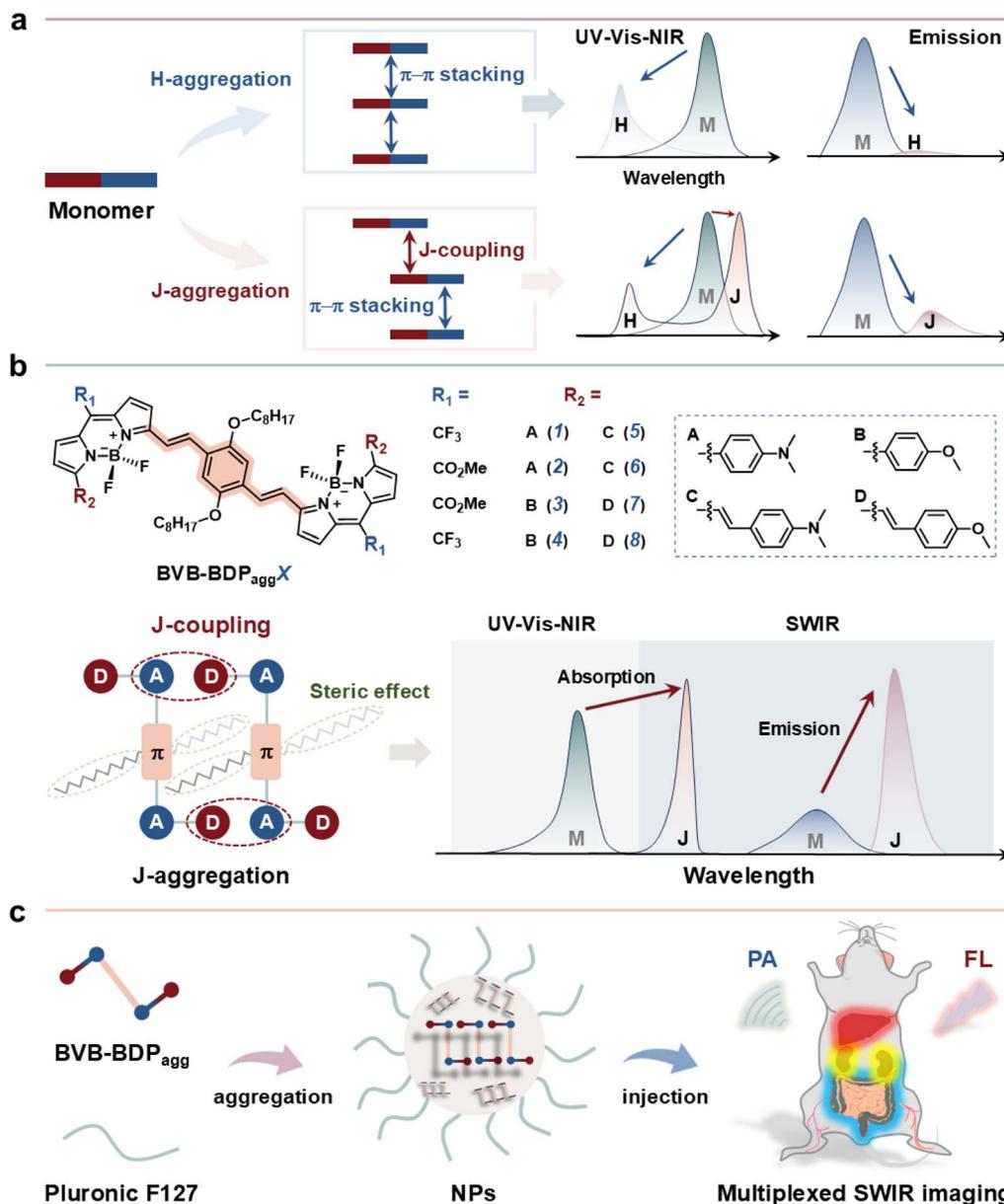
Fig. 1 Molecular structures and working principle. (a) The absorption and emission properties of H- and J-aggregates. (b) Design and chemical structures of BVB-BDP$_{agg}$1–8. (c) Schematic illustration of the preparation of the BVB-BDP$_{agg}$1 and BVB-BDP$_{agg}$5 J-nanoparticles for SWIR fluorescence and photoacoustic imaging.

6 exhibited more intense emission signals beyond 1000 nm compared to BVB-BDP$_{agg}$3–4 and BVB-BDP$_{agg}$7–8, likely due to their relatively enhanced ICT characteristics.[37]

Photophysical properties in the aggregation state

We investigated the aggregation behavior of BVB-BDP$_{agg}$1–8 in various solvents with differing polarities (Fig. S4). All compounds remained monomeric in most solvents, exhibiting a tendency to aggregate in acetonitrile, ethanol, and methanol.

BVB-BDP$_{agg}$1 and BVB-BDP$_{agg}$5 formed J-aggregates in these poor solvents, displaying sharp and narrow J-absorption bands centered around 1020 nm and 1108 nm, respectively. Additionally, shoulder absorption bands were observed at

approximately 865 nm and 922 nm, corresponding to monomeric absorption. Conversely, BVB-BDP$_{agg}$4 formed H-aggregates in these poor solvents, exhibiting broad absorption bands centered approximately at 628 nm. Notably, BVB-BDP$_{agg}$2–3 and BVB-BDP$_{agg}$6–8 formed J-/H-hybrid aggregates, with corresponding J- and H-absorption bands visible in the spectra.

Next, we examined the aggregation behavior of these compounds in tetrahydrofuran (THF)–methanol or THF–acetonitrile binary solvents (Fig. 2a and S5). As the fractions of the methanol or acetonitrile (f_M or f_A) in THF increased, the two monomeric absorption bands gradually diminished, while the J-bands for BVB-BDP$_{agg}$1 and BVB-BDP$_{agg}$5 intensified, centered

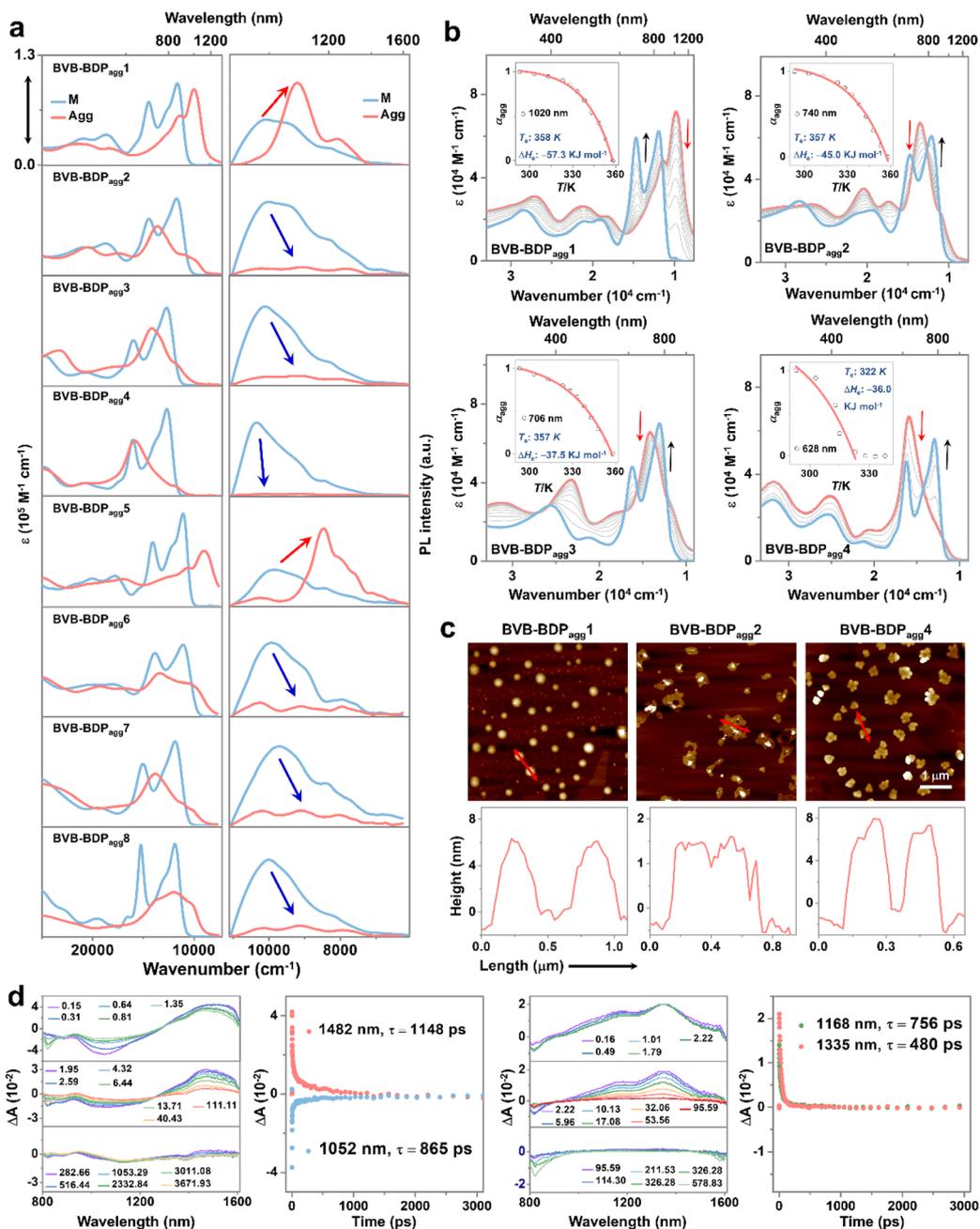Fig. 2 Photophysical properties and aggregation behavior studies. (a) Absorption and emission spectra of BVB-BDP$_{agg}$1–8 and BVB-BDP$_{agg}$1–8 aggregates (10 μM). (b) Temperature-dependent absorption spectra of BVB-BDP$_{agg}$1–4 in EtOH from 293 to 353 K at a total concentration of 10 μM. (c) Atomic force microscopy images of J-aggregates of BVB-BDP$_{agg}$1, J/H-aggregates of BVB-BDP$_{agg}$2 and H-aggregates of BVB-BDP$_{agg}$4 and cross-section analysis along the red lines. (d) Transient absorption difference spectra of J-aggregates of BVB-BDP$_{agg}$1 and H-aggregates of BVB-BDP$_{agg}$4 recorded in MeOH at 298 K, and corresponding transient absorption decay dynamics.

at 1010 nm and 1108 nm. For **BVB-BDP$_{agg}$4,** H-band was centered at 628 nm. **BVB-BDP$_{agg}$2–3** and **BVB-BDP$_{agg}$6–8** exhibited both J- and H-bands, suggesting the coexistence of J- and H-aggregates. The absorption spectrum at f_M or $f_A = 99\%$ closely resembled those obtained in methanol or acetonitrile solutions, further confirming the formation of J- or H-aggregates.

We further investigated the fluorescence properties of the aggregates of **BVB-BDP$_{agg}$1–8** (Fig. 2a and S6). Notably, the J-aggregates of **BVB-BDP$_{agg}$1** and **BVB-BDP$_{agg}$5** exhibited highly emissivity. Increasing the fraction of poor solvents led to a decrease in the monomer emission bands for these compounds. This may be attributed to the aggregates existing in a metastable state between short-range and long-range order, favoring energy release through nonradiative transitions, which

could explain the observed fluorescence quenching. Up reaching 90% solvent fraction, the J-aggregates showed a dramatic enhancement in J-emission bands at 1100 nm for **BVB-BDP$_{agg}$1** and 1200 nm for **BVB-BDP$_{agg}$5**, indicating the formation of long-range ordered J-aggregates and resulting aggregation-induced emission enhancement.

In contrast to the efficient fluorescence of the J-aggregates, the formation of H-aggregates from **BVB-BDP$_{agg}$4** led to significant aggregation-caused fluorescence quenching. **BVB-BDP$_{agg}$2–3** and **BVB-BDP$_{agg}$6–8** exhibited both the emission bands from J- and H-aggregates, however, their fluorescence was distinctly quenching during aggregation. The quantitative results of the Φ_f of monomers and aggregates of **BVB-BDP$_{agg}$1–8** are almost consistent with their spectral behavior changes (Table S2). These results suggest that, when J- and H-aggregates coexist, the emission quenching resulting from H-aggregation dominates the overall fluorescence behavior of the aggregates.

Aggregation behavior studies

To rationalize the diverse aggregation behavior of **BVB-BDP$_{agg}$1–8** and their corresponding photophysical properties, we conducted temperature-dependent UV-Vis-NIR spectroscopic measurements (Fig. 2b, S7–S9 and Table S3). As the temperature increased from 293 K to 358 K, both J- and H-bands of **BVB-BDP$_{agg}$1–8** gradually diminished, accompanied by an increment in monomeric absorption bands. Except for **BVB-BDP$_{agg}$7**, complete dissociation of the aggregates into monomers was observed at about 358 K, as evidenced by the disappearance of J- and H-bands and the presence of only the monomeric absorption band. For **BVB-BDP$_{agg}$7** aggregates, complete dissociation could not be achieved within the temperature range accessible in ethanol solvent.

The full widths at half maxima (FWHM) of J-bands observed in the aggregates of **BVB-BDP$_{agg}$1–3**, **BVB-BDP$_{agg}$6** and **BVB-BDP$_{agg}$8** were narrower than those observed in the first absorption bands of the monomer. In contrast, the H-bands observed in the aggregates of **BVB-BDP$_{agg}$2–4**, **BVB-BDP$_{agg}$6** and **BVB-BDP$_{agg}$8** showed broader FWHM compared to the first absorption bands of the monomers, further confirming the formation of J- and H-aggregates of these compounds. It should be noted that only approximately 62% of **BVB-BDP$_{agg}$5** monomers aggregated into J-aggregates in acetonitrile, resulting in the coexistence of both monomeric and J-aggregate absorption bands in the spectra. Consequently, the FWHM of the J-band was slightly broader than that of the monomer band, suggesting that the J-aggregates formed in acetonitrile were in a metastable state rather than a fully ordered stable-aggregate. The transition dipole moment (μ_{eg}) value for the J-aggregates of **BVB-BDP$_{agg}$1** was calculated to be 10.3 D, slightly higher than that of the monomer (9.8 D), indicating the relative weak J-coupling between the monomers.[38,39] Such moderate J-coupling may contribute the strong SWIR emission profile of the J-aggregates.

We used the nucleation–elongation model to study the aggregation behavior of **BVB-BDP$_{agg}$1–4**, **BVB-BDP$_{agg}$6** and **BVB-BDP$_{agg}$8**.[40] By fitting UV-Vis-NIR spectroscopic data of the fraction of aggregated molecules (α_{agg}) versus temperature (T) (inset in Fig. 2b and S9), we determined the molar enthalpy (ΔH_e) and elongation temperature (T_e) for each aggregate (Table S3). The lower ΔH_e of **BVB-BDP$_{agg}$1** suggests a higher propensity for aggregation. Interestingly, in the J-/H-hybrid aggregates like **BVB-BDP$_{agg}$2**, **BVB-BDP$_{agg}$3**, and **BVB-BDP$_{agg}$6**, we calculated the ΔH_e and T_e for both J- and H-aggregates. While for J-aggregates of D–A structured **BVB-BDP$_{agg}$2** and **BVB-BDP$_{agg}$3**, the T_e are similar for both types of aggregates in **BVB-BDP$_{agg}$2**, **BVB-BDP$_{agg}$3**, the significantly lower ΔH_e for J-aggregates indicates their easier formation. In contrast, **BVB-BDP$_{agg}$6** shows a preference for H-aggregates formation. These results emphasize the crucial role of molecular structure in controlling aggregation behavior.

Next, we characterized the morphology of the aggregates using atomic force microscopy to investigate their structural details (Fig. 2c, S10 and Table S4). **BVB-BDP$_{agg}$1** aggregates had dimensions of 269 ± 57 nm in length, 240 ± 51 nm in width, and 6.2 ± 1.9 nm in height, while **BVB-BDP$_{agg}$5** aggregates had dimensions of 242 ± 34 nm in length, 230 ± 47 nm in width, and 8 ± 2.7 nm in height. Under the same conditions, **BVB-BDP$_{agg}$4** in methanol solution self-assembled into mass-like aggregates with similar dimensions (247 ± 71 nm in length, 173 ± 32 nm in width, and 9.0 ± 1.6 nm in height). Their mass-like morphology likely results from long-range ordered packing structures. In contrast, **BVB-BDP$_{agg}$2–3** and **BVB-BDP$_{agg}$6–8** in methanol solution self-assembled into irregular, flake-like aggregates with larger dimensions (500 ± 150 nm in length, 350 ± 100 nm in width, and 2 ± 1.0 nm in height), possibly due to hybrid J-/H-aggregation favoring short-range disordered packing arrangements.

These results suggest that **BVB-BDP$_{agg}$1**, **BVB-BDP$_{agg}$5** and **BVB-BDP$_{agg}$4** preferentially form highly ordered packing structures. In contrast, the coexistence of J- and H-type packing modes in **BVB-BDP$_{agg}$2–3** and **BVB-BDP$_{agg}$6–8** likely hinders the formation of highly stable, uniformly packed aggregates. These findings are consistent with the temperature-dependent UV-Vis-NIR spectroscopic measurements.

Excited state dynamics

We performed femtosecond transient absorption spectroscopy (fs-TAS) to elucidate the excited state dynamics of J- and H-aggregates. **BVB-BDP$_{agg}$1–4** aggregates were selected as representatives and their transient absorption spectra are shown in Fig. 2d, S11 and S12.

For J-aggregates of **BVB-BDP$_{agg}$1**, we observed a ground-state bleaching (GSB) band at 1052 nm and an excited-state absorption (ESA) feature centered at 1482 nm within the 800–1620 nm spectral range. The ESA decays within the first 1 ps, attributed to solvation and structural relaxation. Subsequently, both the ESA and GSB signals decay near baseline with an isosbestic point at 1261 nm, and the lifetimes of the GSB and ESA were calculated to be approximately 865 ps and 1148 ps, respectively.

In contrast, the ESA signals of the aggregates **BVB-BDP$_{agg}$2** (at 1355 and 1464 nm), **BVB-BDP$_{agg}$3** (at 1185 and 1291 nm) and **BVB-BDP$_{agg}$4** (at 1168 and 1335 nm) exhibit faster quenching

from approximately 2.00 to 50.00 ps, with significantly shorter calculated lifetimes compared to **BVB-BDP$_{agg}$1** J-aggregates (Fig. 2d and S12). This relatively rapid excited-state quenching suggests stronger intermolecular interactions and exciton effects in the aggregates of **BVB-BDP$_{agg}$2–4** compared to **BVB-BDP$_{agg}$1**, rationalizing the intense fluorescence properties of **BVB-BDP$_{agg}$1** J-aggregates and the quenched fluorescence profiles of **BVB-BDP$_{agg}$2–4** aggregates under steady-state conditions.

Notably, J-aggregates of **BVB-BDP$_{agg}$1** and H-aggregates of **BVB-BDP$_{agg}$4** exhibit a distinct isosbestic point during decay, indicating the presence of a unique excited-state species. In contrast, the shifted isosbestic point in the transient absorption spectra of **BVB-BDP$_{agg}$2** and **BVB-BDP$_{agg}$3** aggregates suggests the coexistence of J- and H-type excimers.

X-ray crystallographic analysis

To investigate the relationship between the aggregation behavior and the photophysical properties, we conducted the X-ray crystallographic analysis (Fig. 3 and S2). Single-crystal analysis revealed a *trans* conformation for all compounds, confirming the proposed "zigzag" structure. The BODIPY core and 1,4-bisvinylbenzene unit were well-planned in the crystalline state. However, the *p*-methoxyphenyl and *p*-dimethylaminophenyl groups at the 5,5′-positions exhibited slight deviations from the plane due to steric hindrance from the octyl groups.

BVB-BDP$_{agg}$1 exhibits a typical J-type packing structure, where each monomer is interconnected through CT interactions between the nitrogen atom in the *p*-dimethylaminophenyl group and the BODIPY core in a "head-to-tail" fashion, with a distance of approximately 3.45 Å (Fig. 3a). Notably, no other strong intermolecular interactions, such as π–π stacking or hydrogen bonding, were observed within this packing structure, aside from the CT interactions.

BVB-BDP$_{agg}$2 and **BVB-BDP$_{agg}$3** display a hybrid J- and H-type packing structure. In **BVB-BDP$_{agg}$2**, CT interactions between the *p*-dimethylaminophenyl group and the BODIPY core are present, with a distance of 3.64 Å, slightly longer than that in the J-aggregates of **BVB-BDP$_{agg}$1**. Conversely, due to the relatively poor electron-donating ability of the *p*-methoxyphenyl group, the BODIPY core in **BVB-BDP$_{agg}$3** preferentially interacts with the benzene ring of the 1,4-bisvinylbenzene bridge, with a distance of around 3.47 Å. Additionally, the increased π-conjugation induced by the –CO$_2$Me group facilitates π–π stacking and C–H···O hydrogen bonding between the BODIPY cores in these two compounds.

In contrast to the J- or hybrid J-/H-type packing observed in **BVB-BDP$_{agg}$1–3**, only π–π stacking (3.47 Å) is present in the packing structure of **BVB-BDP$_{agg}$4**. This suggests a relatively weak CT interaction between the CF$_3$-BODIPY core and the *p*-methoxyphenyl group as well as the 1,4-bisvinylbenzene bridge.

The crystallographic analysis results correlate well with the observed photophysical properties in the aggregation state. The bathochromic-shifted absorption and increased emission of **BVB-BDP$_{agg}$1** J-aggregates can be attributed to the exclusive J-

coupling in its molecular packing. In contrast, the H-type packing mode in **BVB-BDP$_{agg}$4** leads to hypochromic-shifted absorption and emission quenching. The presence of both J- and H-bands in the absorption spectrum of **BVB-BDP$_{agg}$2** and **BVB-BDP$_{agg}$3** reflects their hybrid packing modes. Consequently, the distinctive J-coupling, free from interference from other intermolecular interactions, is crucial for the intense absorption and fluorescence observed in **BVB-BDP$_{agg}$1** J-aggregates. The hybridization of H-coupling with J-coupling results in the simultaneous appearance of J- and H-bands in the absorption spectrum, as well as bathochromic-shifted and quenched emission.

In vitro imaging ability

To efficiently collect emitted photons and optimize signal detection for high-resolution SWIR imaging, the use of long-pass (LP) filters is crucial.[1,9] To assess the potential of **BVB-BDP$_{agg}$1** and **BVB-BDP$_{agg}$5** J-aggregates for SWIR imaging with different LP filters, we first calculated their SWIR brightness by multiplying the Φ_f by the absorption coefficient (Table S2). Amongst the monomers and aggregates of **BVB-BDP$_{agg}$1** and **BVB-BDP$_{agg}$5**, **BVB-BDP$_{agg}$1** exhibited the highest SWIR brightness of approximately 2736 M^{-1} cm^{-1}.

We then comparatively investigated the imaging capabilities of these J-aggregates using incrementally bathochromic-shifted LP filters ranging from 1000 to 1300 nm. For comparison, we also included several reported and commercially available SWIR dyes, including NJ1060,[17] IR1061,[41] and ICG.[42] By preparing solutions with equal concentrations at the excitation wavelength of 808 nm and measuring differences in emission intensity as a function of LP filter, we could determine and compare these values.

As shown in Fig. 4a and S13, when using 1000 nm and 1100 nm filters, all test samples except for IR1061 showed intense signals. Although the absorption of **BVB-BDP$_{agg}$1** and **BVB-BDP$_{agg}$5** J-aggregates at 808 nm is not their absorption maximum, their imaging quantification intensities were even slightly larger than those of NJ1060, IR1061, and ICG, indicating their highly fluorescent profiles. As the LP filter wavelength increased, the imaging intensity of **BVB-BDP$_{agg}$5** J-aggregates remained relatively unchanged, while other examples showed significantly decreased intensity. This reflects the superior brightness imaging advantage of the 1200 nm fluorescence emission of **BVB-BDP$_{agg}$5** J-aggregates.

We also studied the effect of excitation wavelength on imaging performance under the same conditions. As the excitation wavelength increased from 808 to 980 nm, **BVB-BDP$_{agg}$1** and **BVB-BDP$_{agg}$5** J-aggregates exhibited improved imaging performance compared to other test samples. When using a 1064 nm excitation wavelength, only the emission of **BVB-BDP$_{agg}$1** and **BVB-BDP$_{agg}$5** J-aggregates was observed due to their unique SWIR absorption properties. Moreover, the emission intensity of **BVB-BDP$_{agg}$5** J-aggregates was approximately 1.7-fold higher than that of **BVB-BDP$_{agg}$1** J-aggregates, demonstrating the pronounced imaging ability of **BVB-BDP$_{agg}$5** J-
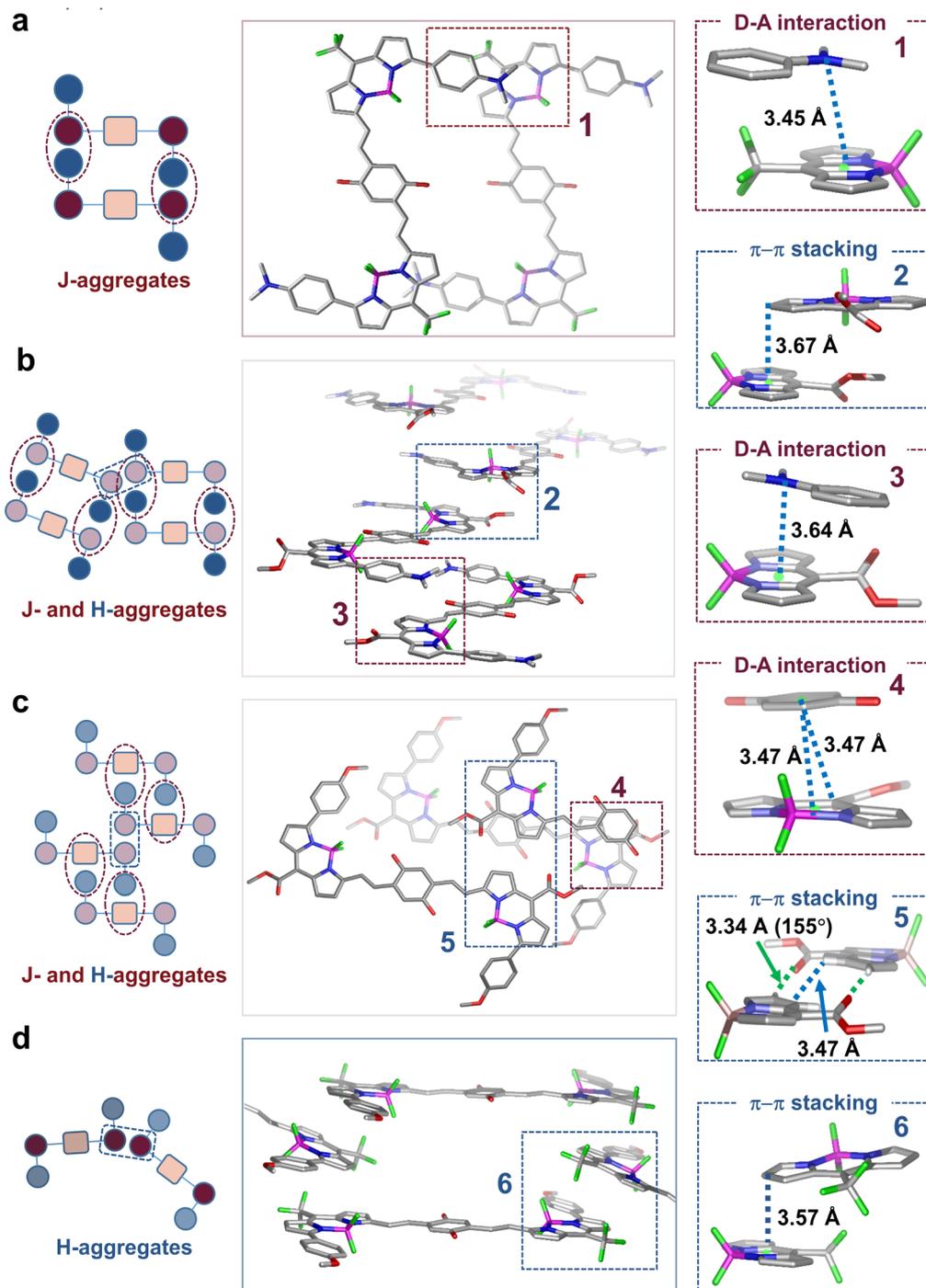
Fig. 3 X-ray crystallographic analysis. Molecular packing diagrams of **BVB-BDP$_{agg}$1** (a, J-type), **BVB-BDP$_{agg}$2** (b, J- and H-hybrid), **BVB-BDP$_{agg}$3** (c, J- and H-hybrid) and **BVB-BDP$_{agg}$4** (d, H-type) in the crystalline state. Intermolecular interactions and the related data in the molecular packing structures are presented on the right as 1–6.

aggregates compared to **BVB-BDP$_{agg}$1** J-aggregates as well as other tested samples.

Considering that SWIR fluorescent agents often exhibit PA imaging ability due to increased non-radiative decay in the SWIR region,[4,43,44] we further investigated the PA imaging performance of **BVB-BDP$_{agg}$1** and **BVB-BDP$_{agg}$5** J-aggregates. We include **BVB-BDP$_{agg}$1** monomer and **BVB-BDP$_{agg}$4** H-aggregates,

which exhibit λ_{abs} in NIR region for comparison (Fig. 4b and S14). Upon excitation with 680 nm laser, **BVB-BDP$_{agg}$4** H-aggregates showed the strongest PA signals among the four samples, suggesting that H-aggregation enhances the PA effect. The relatively poor PA imaging ability of **BVB-BDP$_{agg}$1** and **BVB-BDP$_{agg}$5** J-aggregates can be attributed to their weak absorption in NIR region. As the laser wavelength increased to 850 and
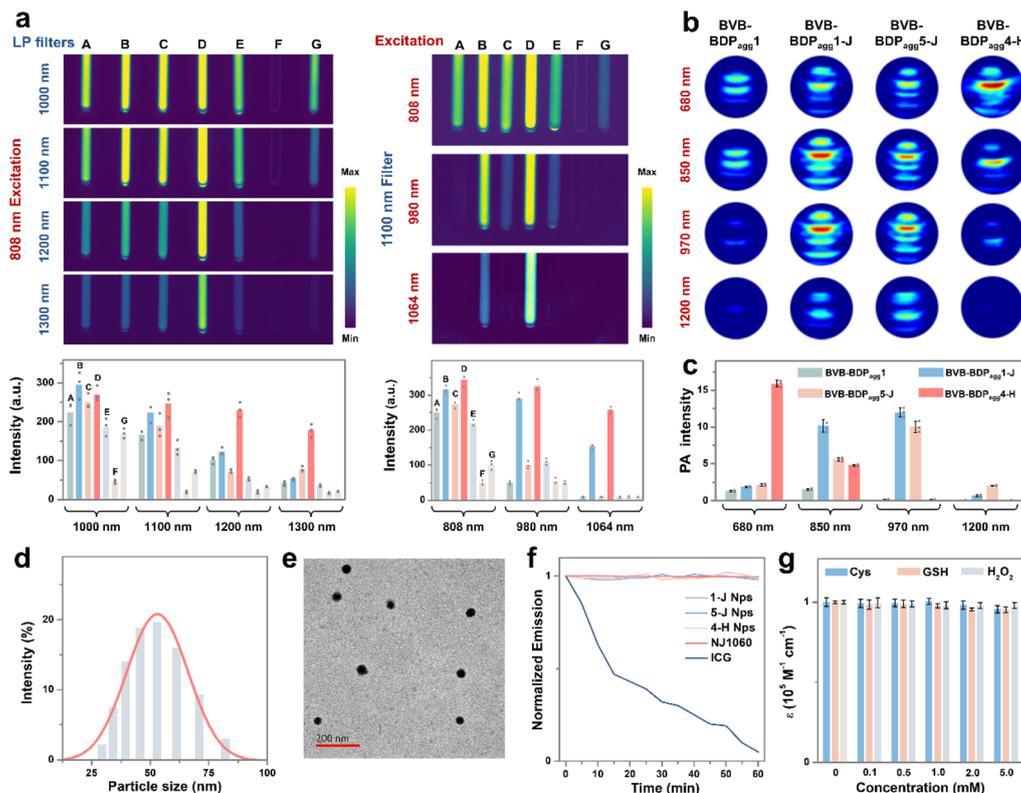
Fig. 4 *In vitro* imaging and NPs characterization. (a) Left: Capillary images of various dyes (10 μM) under 808 nm excitation. Right: Capillary images of various dyes (10 μM) with the same LP filters under different excitation. (A) BVB-BDP$_{agg}$1; (B) BVB-BDP$_{agg}$1 J-aggregates; (C) BVB-BDP$_{agg}$5; (D) BVB-BDP$_{agg}$5 J-aggregates; (E) NJ1060; (F) IR1061 and (G) ICG. (b) PA imaging ability of monomers and J-aggregates of BVB-BDP$_{agg}$1 and BVB-BDP$_{agg}$5 J-aggregates, and BVB-BDP$_{agg}$4 H-aggregates under different excitation wavelengths. (c) Quantified PA intensity from 4b. (d) Particle size distribution of BVB-BDP$_{agg}$1 NPs measured by DLS. (e) TEM image of BVB-BDP$_{agg}$1 NPs, scale bar, 200 nm. (f) and (g) Photo-stability of BVB-BDP$_{agg}$1 NPs, BVB-BDP$_{agg}$5 NPs and BVB-BDP$_{agg}$4 NPs and chem-stability of BVB-BDP$_{agg}$1 NPs.

970 nm, the PA signal of BVB-BDP$_{agg}$1 and H-aggregates of BVB-BDP$_{agg}$4 decreased, probably due to the reduced absorption in this region. In contrast, the PA signal of BVB-BDP$_{agg}$1 and BVB-BDP$_{agg}$5 J-aggregates gradually increased because of their well-matched absorption band to the excitation wavelength. When the excitation wavelength was further bathochromically shifted to 1200 nm, only the PA signals of BVB-BDP$_{agg}$1 and BVB-BDP$_{agg}$5 J-aggregates were observed, highlighting their superior PA imaging ability in the SWIR region.

To further analyze these findings, we fitted the PA full spectra of BVB-BDP$_{agg}$1 monomers, BVB-BDP$_{agg}$1 J-aggregates, BVB-BDP$_{agg}$5 J-aggregates, and BVB-BDP$_{agg}$4 H-aggregates (Fig. 4c and S15). The fitted spectra closely aligned with the corresponding absorption spectra, providing a rational explanation for the observed differences in PA imaging performance.

Encouraged by the SWIR emission and PA imaging ability of J-aggregates of BVB-BDP$_{agg}$1 and BVB-BDP$_{agg}$5, and H-aggregates of BVB-BDP$_{agg}$4, we investigated the potential for stabilizing these nanoparticles (NPs) for *in vivo* imaging. We prepared BVB-BDP$_{agg}$1 NPs, BVB-BDP$_{agg}$5 NPs and BVB-BDP$_{agg}$4 NPs by encapsulating the aggregates into a Pluronic F-127 matrix.[31]

The BVB-BDP$_{agg}$1 NPs were found to be spherical with an average diameter of approximately 53 nm, as characterized by

dynamic light scattering (DLS) and transmission electron microscopy (TEM) (Fig. 4d and e). BVB-BDP$_{agg}$5 NPs and BVB-BDP$_{agg}$4 NPs exhibited similar morphologies and sizes, with average diameters of approximately 79 and 73 nm, respectively (Fig. S16). As shown in Fig. S17, BVB-BDP$_{agg}$1 NPs and BVB-BDP$_{agg}$5 NPs displayed absorption wavelength at 1030 nm ($\varepsilon = 91\,000$ M^{-1} cm^{-1}) and 1095 nm ($\varepsilon = 85\,000$ M^{-1} cm^{-1}), respectively, consistent with the results obtained in the methanol and acetonitrile. Additionally, the emission wavelengths of these two NPs in aqueous solution were approximately 1108 and 1193 nm, respectively. These results suggest that the J-aggregates of BVB-BDP$_{agg}$1 and BVB-BDP$_{agg}$5 are well-stabilized in the Pluronic F-127 matrix.

Importantly, the BVB-BDP$_{agg}$1 NPs and BVB-BDP$_{agg}$5 NPs exhibited relatively high Φ_f in PBS buffer, with measured Φ_f values of 2.5 ± 0.6% and 2.3 ± 0.3%, respectively. These values exceed those of most reported SWIR emissive cyanine dyes, as well as J-aggregates such as IR1061 and FD-1080.[5] In contrast, the hypsochromic-shifted absorption wavelength (632 nm, $\varepsilon = 89\,000$ M^{-1} cm^{-1}) and nearly non-luminescent properties of BVB-BDP$_{agg}$4 NPs indicate that the encapsulated NPs primarily from H-aggregates. Notably, the high ε of these NPs is comparable to the reported J-/H-aggregates based on cyanine, indicating their efficient photoabsorption ability.

Furthermore, we assessed the photostability of **BVB-BDP$_{agg}$1** NPs, **BVB-BDP$_{agg}$5** NPs and **BVB-BDP$_{agg}$4** NPs, comparing them with SWIR dyes NJ1060 and ICG. After continuous laser irradiation (808 nm, 400 mW cm^{-2}) for 60 min, the SWIR emission intensities of these three NPs and NJ1060 remained almost unchanged, while the fluorescence intensity of ICG decreased significantly from 100% to 7% under the same conditions (Fig. 4f). Moreover, **BVB-BDP$_{agg}$1** NPs, **BVB-BDP$_{agg}$5** NPs and **BVB-BDP$_{agg}$4** NPs showed no significant changes in their absorption, PA and fluorescence spectra in PBS after incubation with glutathione (GSH), cysteine (Cys), and hydrogen peroxide (H$_2$O$_2$) for 6 h (Fig. 4g and S18–S20). In addition, these three types of NPs exhibit a more stable PA signal than that of clinically used ICG after exposure to a pulsed laser, which demonstrates the suitability of these NPs for long-term PA imaging (Fig. S21). These results highlight the excellent stability of these NPs, making them promising candidates for further *in vivo* imaging applications.

In vivo SWIR imaging

To verify the high-resolution biological imaging ability of these NPs, we carried out *in vivo* imaging experiments. Before *in vivo* SWIR imaging, we first examined the *in vitro* fluorescence penetration depth of **BVB-BDP$_{agg}$1** NPs, **BVB-BDP$_{agg}$5** NPs. As shown in Fig. S22 and S23, **BVB-BDP$_{agg}$1** NPs achieve a tissue penetration depth of 6 mm in chicken breast tissue, while **BVB-BDP$_{agg}$5** NPs reach a penetration depth of up to 10 mm, which demonstrates their high imaging depth. In addition, we first assessed the biocompatibility of **BVB-BDP$_{agg}$1** NPs in living cells and mice. **BVB-BDP$_{agg}$1** NPs exhibited negligible toxicity in both normal and cancerous cells (Fig. S24). The hepatic function analyses and blood tests of healthy mice after injection of **BVB-BDP$_{agg}$1** NPs also show no significant abnormalities (Fig. S25 and S26). These results further supported the biological safety of these NPs for *in vivo* imaging applications. Then, we tested the most promising J-aggregates NPs, **BVB-BDP$_{agg}$1** and **BVB-BDP$_{agg}$5** for single-color mouse imaging *via* intravenous (i.v.) injection.

We injected **BVB-BDP$_{agg}$1** NPs into mice and immediately performed non-invasive *in vivo* SWIR fluorescence imaging with 980 nm excitation and 1100 nm LP filter (Fig. 5a and S27). The blood vessels in both the abdominal area and hindlimb were visualized with high resolution against the surrounding tissue. When using **BVB-BDP$_{agg}$5** NPs under the same conditions, the enhanced resolution in the SWIR region was apparent, as confirmed by quantitative analysis. Specifically, the full width at half maximum of the emission intensity profiles in the region of interest (ROI) indicated that the diameter of the blood vessels was estimated to be 0.41 mm, significantly smaller than that observed with **BVB-BDP$_{agg}$1** NPs. After 1 min, both **BVB-BDP$_{agg}$1** and **BVB-BDP$_{agg}$5** NPs began to accumulate in the liver and spleen, consistent with the behavior of most reported small organic molecular-based SWIR dyes (Fig. S28).[10,14,42]

Given the distinct differences in absorption and emission wavelengths between **BVB-BDP$_{agg}$1** NPs and **BVB-BDP$_{agg}$5** NPs, we proceeded to conduct *in vivo* multiplexed imaging. We

injected **BVB-BDP$_{agg}$1** NPs intraperitoneally (i.p.) into a mouse and observed a strong fluorescence signal with a 1200 nm LP filter under 980 nm excitation (Fig. 5b). Subsequently, we intravenously injected **BVB-BDP$_{agg}$5** NPs into the same mouse and used 1064 nm excitation to simultaneously visualize the vasculature and intraperitoneal cavity in the high-resolution SWIR region. Over time, **BVB-BDP$_{agg}$5** NPs predominantly accumulated in the liver. We then demonstrated orthogonal detection (Fig. 5c) and quantified the signal across an ROI for both the 980 nm and 1064 nm channels (Fig. 5d). Notably, two-color fluorescence signals were clearly distinguishable. These results indicated that **BVB-BDP$_{agg}$1** NPs and **BVB-BDP$_{agg}$5** NPs have significant potential for excitation-based multiplexing imaging.

Given the potential for enhanced PA signals from aggregates, we also investigated *in vivo* multiplexed PA tomography imaging. We selected **BVB-BDP$_{agg}$4** NPs, H-aggregates with a 680 nm absorption wavelength, to avoid crosstalk with the PA signals from **BVB-BDP$_{agg}$1** NPs and **BVB-BDP$_{agg}$5** NPs. We mixed equal concentrations of **BVB-BDP$_{agg}$1**, **BVB-BDP$_{agg}$5** and **BVB-BDP$_{agg}$4** NPs and injected them intravenously into mice. We then performed 3D high-resolution PA imaging sequentially at 680 nm, 850 nm, and 1064 nm channels (Fig. 5e). Compared to the control group, the PA signals across all three channels were significantly enhanced (Fig. S29).

As shown in Fig. 5f, at the 680 nm channel, the PA signals from **BVB-BDP$_{agg}$4** NPs were primarily localized to blood vessels, with a quantified blood vessel diameter of approximately 0.28 mm. **BVB-BDP$_{agg}$1** NP signals at 850 nm were predominantly observed in the liver and spleen, as confirmed by cross-sectional tomography (Z_1). These findings, combined with fluorescence imaging, indicate that **BVB-BDP$_{agg}$1** NPs are primarily metabolized by the liver after approximately 25 minutes of circulation. Finally, we analyzed the PA signal of **BVB-BDP$_{agg}$5** NPs in the 1064 nm channel. Aside from a minor signal in the liver, PA signals were predominantly distributed in the kidneys and intestines (Z_2 and Z_3). This suggests that **BVB-BDP$_{agg}$5** NPs are mainly metabolized through the kidneys and intestines after circulating in the body for about 50 minutes. Importantly, the three-color composite image provides a comprehensive overview of the differential bio-distribution of the three nanoparticles, highlighting their capacity for high-resolution *in vivo* PA imaging.

Recent advances in multimodal imaging and biological species 3D imaging will further expand the application scope of imaging agents in life science.[45,46] To further expand the *in vivo* applications of these J-aggregates NPs, we also explored their capability for fluorescence/photoacoustic imaging-guided photothermal therapy (PTT) in tumor-bearing mice. Taking **BVB-BDP$_{agg}$1** NPs as an example, we first examined its *in vitro* photothermal performance before proceeding to *in vivo* experiments.

As shown in Fig. S30, under 1064 nm laser light irradiation (0.75 W cm^{-2}), the temperature of **BVB-BDP$_{agg}$1** NPs solution showed dramatically increasing profiles (Fig. S30a). After irradiation for 10 min, NPs solution rapidly increased the temperature from 29 °C to 56 °C. Under the same conditions, pure PBS
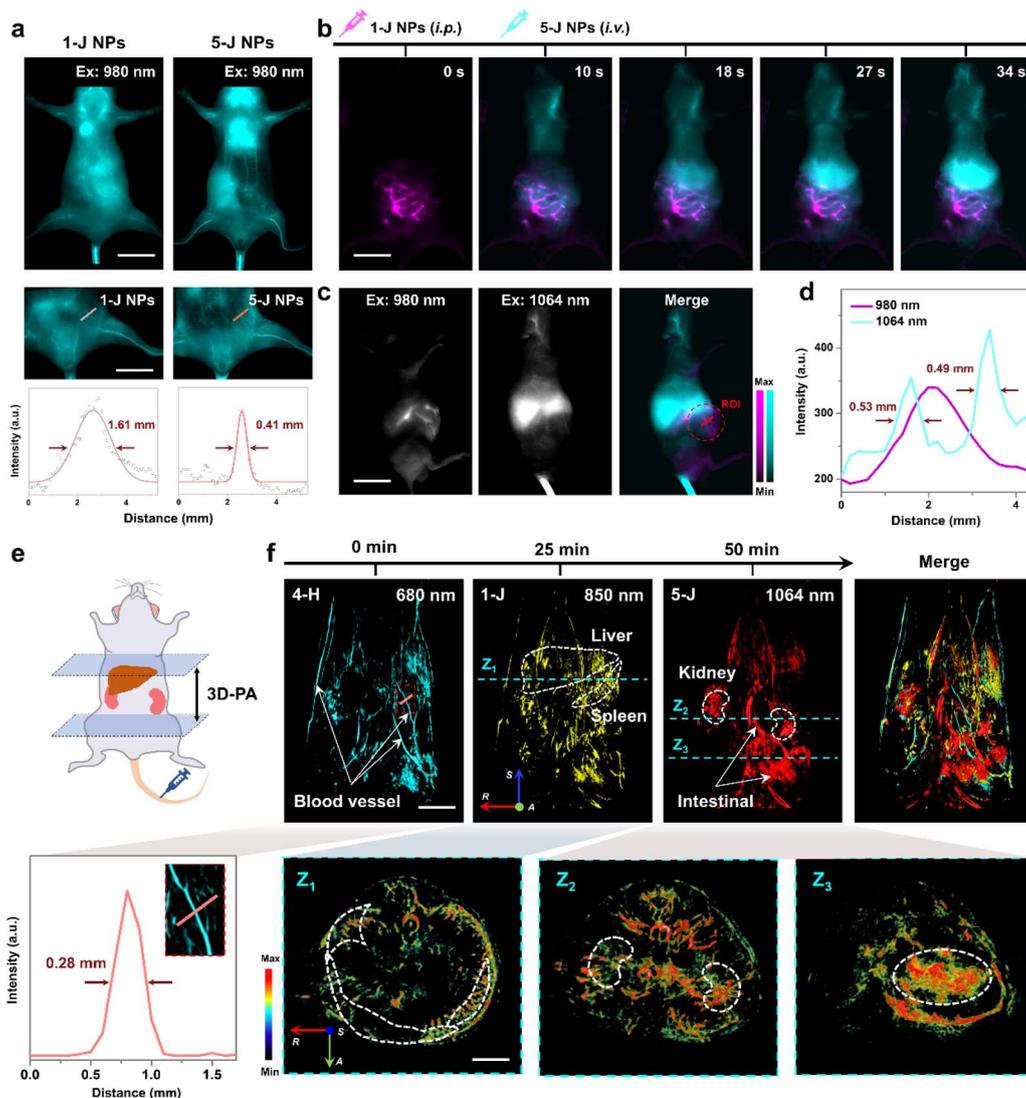
Fig. 5 *In vivo* fluorescence and PA imaging. (a) SWIR images and the quantification of fluorescent signals of the mouse after tail vein injection of **BVB-BDP$_{agg}$1** NPs and **BVB-BDP$_{agg}$5** NPs upon a 980 nm laser, scale bar: 10 mm. (b) Representative 2-color *in vivo* imaging over the course of 35 seconds; 1200 LP, scale bar = 10 mm. (c) Side-view 980 and 1064 nm imaging channels and ROI, scale bar = 10 mm. (d) Plotted intensity for 980 and 1064 nm channels from (c). (e) Schematic diagram of the PA imaging site of mice. (f) *In vivo* multi-color PA imaging, corresponding quantification data and cross-sectional tomography imaging, scale bar = 5 and 3 mm, respectively. A, anterior; S, superior; and R, right.

solution increased the temperature from 29 °C to 34 °C. Corresponding infrared images are shown in Fig. S30b. According to the change in the temperature, the photothermal conversion efficiency (PCE) values of **BVB-BDP$_{agg}$1** NPs were calculated to be 51% (Fig. S30c). It is noteworthy that the NPs showed negligible degradation after six heating and cooling cycles under laser irradiation, demonstrating excellent thermal- and photo-stability.

Next, we performed *in vivo* PA and SWIR fluorescence imaging of 4T1 tumor-xenografted mice injected with the **BVB-BDP$_{agg}$1** NPs in PBS (150 μL, 100 μM) at the tail vein, the fluorescence and PA images of mice at different times were recorded. As shown in Fig. 6a, b and S31, the fluorescence and PA signal from the tumor increases to a maximum at 10 h post-injection and then gradually vanishes. These results suggest

that **BVB-BDP$_{agg}$1** NPs have good tumor-targeting and imaging performance. The *in vivo* PTT efficacy of **BVB-BDP$_{agg}$1** NPs was further evaluated in 4T1 tumor-bearing BALB/c mice (∼130 mm^3). Following intravenous injection (150 μL, 100 μM) and 1064 nm laser irradiation (0.75 W cm^{-2}, 10 min), infrared thermal imaging revealed a rapid tumor temperature increase from 36 °C to 48 °C in NPs-treated mice, confirming efficient photothermal conversion (Fig. 6c and d).

We next studied the *in vivo* PTT performance by monitoring tumor growth over 16 days (Fig. 6e). Mice bearing ∼130 mm^3 tumors were randomized into four groups: PBS, PBS + laser, NPs, and NPs + laser. In the three groups including PBS, PBS + laser, NPs showed comparable growth rates, reaching ∼8 times the initial volume, indicating negligible effects from laser exposure or NPs administration alone. In contrast, tumors in
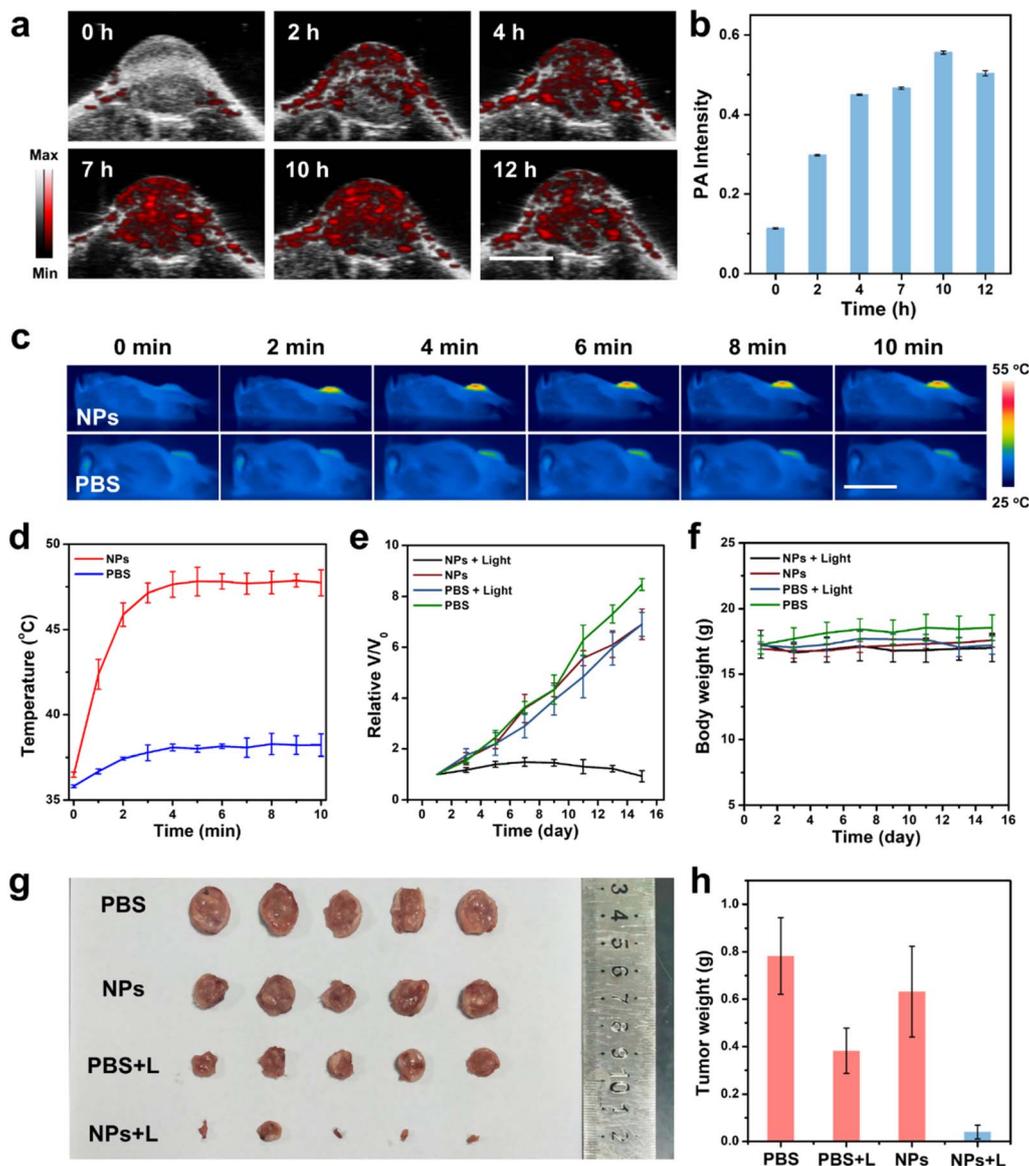
Fig. 6 *In vivo* PA imaging-guided PTT. (a) PA images of the 4T1-tumor at different times postinjection of **BVB-BDP$_{agg}$1** NPs at the tail vein, scale bar: 2 mm. (b) PA intensity from (a) plotted as a function of time postinjection. (c) Infrared thermal imaging of 4T1 tumor-bearing mice treated with PBS and **BVB-BDP$_{agg}$1** NPs exposed to 1064 nm laser (0.75 W cm^{-2}) recorded at different time intervals, respectively, scale bar: 10 mm. (d) Temperature profiles of tumor-site as a function of irradiation time. (e) Relative tumor volume (V/V_0) changes of each group during treatments. (f) Body weight changes of mice during different treatments. (g) Photographs of tumors from various treated groups. (h) Average weights of tumors at day 16 after treatment.

the NPs + laser group were completely eradicated with no recurrence observed during the 16 days post-treatment period, demonstrating the outstanding PTT efficacy of **BVB-BDP$_{agg}$1** NPs. During the treatment period, NPs-treated mice maintained stable body weights, demonstrating minimal systemic toxicity (Fig. 6f). Post-treatment dissection revealed significantly smaller tumor volumes in the NPs + laser group compared to other groups, further confirming the potent PTT effect (Fig. 6g and h). Moreover, the tumor apoptosis was further analyzed through H&E staining and TUNEL assays. As shown in Fig. S32, the NPs + laser group exhibited distinct necrotic regions, while other treatment groups showed minimal cellular changes. The

above results revealed the high *in vivo* PTT efficacy of **BVB-BDP$_{agg}$1** NPs.

Conclusions

In summary, we report a robust strategy for tuning the SWIR absorption and emission properties of J-aggregates through zigzag molecular design. A series of 1,4-bisvinylbenzene-bridged zigzag BODIPY dimers, equipped with tunable electron-donating and electron-accepting groups, as well as alkyl chains were synthesized, enabling precise control over J-, H-, and hybrid J-/H-aggregation modes. Notably, the resulting J-

aggregates displayed promising SWIR absorption and emission, with ε and Φ_f reaching 10^5 M^{-1} cm^{-1} and $3.8 \pm 0.6\%$, respectively. Mechanistic studies indicate that the synergistic regulation of intermolecular D–A coupling and steric hindrance effects is key to achieving intense SWIR absorption and emission in J-aggregates. *In vivo* and *in vitro* fluorescence and PA imaging experiments demonstrated that the obtained J-aggregates possess excellent SWIR imaging abilities, with brightness far exceeding those of commercial cyanine probes. Furthermore, we selected different aggregates to achieve multiplexed imaging, demonstrating the superior *in vivo* imaging capabilities of these aggregates. Moreover, we also revealed the great potential of J-aggregates nanoparticles in photoacoustic imaging-guided photothermal therapy. The results from this fundamental research offer insights into the development of J-aggregates with intense SWIR absorption and emission profiles, effectively mitigating fluorescence quenching caused by H-aggregation and strong intermolecular interactions. Additionally, this work paves the way for manipulating the photophysical properties of SWIR dyes for potential applications in biomedical imaging and therapy.

Ethical statement

This study was performed in strict accordance with the guidelines for the care and use of laboratory animals and was approved by the Animal Ethical and Welfare Committee of NJU (Nanjing, China).

Author contributions

Z. Jiang and Z. Liu designed the study. Z. Jiang, X. Ma, T. Wang, M. Dong, and H. Liu synthesized the molecules. Z. Jiang, X. Ma, K. Song, T. Wang, and H. Gao carried out the photochemical experiments and analyzed the corresponding data. Z. Jiang and X. Ma performed the *in vivo* imaging and PTT experiments. Z. Jiang and Z. Liu wrote the manuscript. X. Wang, J. Zhao, and H. Gao conceived the project and revised the manuscript. All authors discussed the results, provided feedback, and approved the final version of the manuscript.

Conflicts of interest

Authors declare that they have no competing interests.

Data availability

CCDC 2401346–2401349 (**BVB-BDP$_{agg}$1–4**) contain the supplementary crystallographic data for this paper.[47]

Supplementary information: The data supporting this article have been included as part of the SI: detailed synthetic procedures; chemical characterization: experimental sections and data; photophysical evaluation: experimental sections and data; biological evaluation: experimental sections and data; and *in vivo* imaging: experimental sections and data. See DOI: **https://doi.org/10.1039/d5sc03864b**.

References

1 Y. Chen, S. Wang and F. Zhang, Near-infrared luminescence high-contrast in vivo biomedical imaging, *Nat. Rev. Bioeng.*, 2023, **1**, 60–78.

2 W. E. Meador, E. Y. Lin, I. Lim, H. C. Friedman, D. Ndaleh, A. K. Shaik, N. I. Hammer, B. Q. Yang, J. R. Caram, E. M. Sletten and J. H. Delcamp, Silicon-RosIndolizine fluorophores with shortwave infrared absorption and emission profiles enable in vivo fluorescence imaging, *Nat. Chem.*, 2024, **16**, 970–978.

3 C. Li, G. Chen, Y. Zhang, F. Wu and Q. Wang, Advanced Fluorescence Imaging Technology in the Near-Infrared-II Window for Biomedical Applications, *J. Am. Chem. Soc.*, 2020, **142**, 14789–14804.

4 J. Huang and K. Pu, Activatable Molecular Probes for Second Near-Infrared Fluorescence, Chemiluminescence, and Photoacoustic Imaging, *Angew. Chem., Int. Ed.*, 2020, **59**, 11717–11731.

5 Z. Lei and F. Zhang, Molecular Engineering of NIR-II Fluorophores for Improved Biomedical Detection, *Angew. Chem., Int. Ed.*, 2021, **60**, 16294–16308.

6 H. Dai, Q. Shen, J. Shao, W. Wang, F. Gao and X. Dong, Small Molecular NIR-II Fluorophores for Cancer Phototheranostics, *Innovation*, 2021, **2**, 100082.

7 S. Zhu, R. Tian, A. L. Antaris, X. Chen and H. Dai, Near-Infrared-II Molecular Dyes for Cancer Imaging and Surgery, *Adv. Mater.*, 2019, **31**, e1900321.

8 E. D. Cosco, A. L. Spearman, S. Ramakrishnan, J. G. P. Lingg, M. Saccomano, M. Pengshung, B. A. Arus, K. C. Y. Wong, S. Glasl, V. Ntziachristos, M. Warmer, R. R. McLaughlin, O. T. Bruns and E. M. Sletten, Shortwave infrared polymethine fluorophores matched to excitation lasers enable non-invasive, multicolour in vivo imaging in real time, *Nat. Chem.*, 2020, **12**, 1123–1130.

9 E. D. Cosco, B. A. Arus, A. L. Spearman, T. L. Atallah, I. Lim, O. S. Leland, J. R. Caram, T. S. Bischof, O. T. Bruns and E. M. Sletten, Bright Chromenylium Polymethine Dyes Enable Fast, Four-Color In Vivo Imaging with Shortwave Infrared Detection, *J. Am. Chem. Soc.*, 2021, **143**, 6836–6846.

10 H. M. Pan, C. C. Wu, C. Y. Lin, C. S. Hsu, Y. C. Tsai, P. Chowdhury, C. H. Wang, K. H. Chang, C. H. Yang, M. H. Liu, Y. C. Chen, S. P. Su, Y. J. Lee, H. K. Chiang, Y. H. Chan and P. T. Chou, Rational Design of Asymmetric Polymethines to Attain NIR(II) Bioimaging at >1100 nm, *J. Am. Chem. Soc.*, 2023, **145**, 516–526.

11 A. L. Antaris, H. Chen, K. Cheng, Y. Sun, G. Hong, C. Qu, S. Diao, Z. Deng, X. Hu, B. Zhang, X. Zhang, O. K. Yaghi, Z. R. Alamparambil, X. Hong, Z. Cheng and H. Dai, A small-molecule dye for NIR-II imaging, *Nat. Mater.*, 2016, **15**, 235–242.

12 Q. Yang, H. Ma, Y. Liang and H. Dai, Rational Design of High Brightness NIR-II Organic Dyes with S-D-A-D-S Structure, *Acc. Mater. Res.*, 2021, **2**, 170–183.

13 H. Shen, F. Sun, X. Zhu, J. Zhang, X. Ou, J. Zhang, C. Xu, H. H. Y. Sung, I. D. Williams, S. Chen, R. T. K. Kwok, J. W. Y. Lam, J. Sun, F. Zhang and B. Z. Tang, Rational Design of NIR-II AIEgens with Ultrahigh Quantum Yields for Photo- and Chemiluminescence Imaging, *J. Am. Chem. Soc.*, 2022, **144**, 15391–15402.

14 D. Liu, Z. He, Y. Zhao, Y. Yang, W. Shi, X. Li and H. Ma, Xanthene-Based NIR-II Dyes for In Vivo Dynamic Imaging of Blood Circulation, *J. Am. Chem. Soc.*, 2021, **143**, 17136–17143.

15 R. Wei, Y. Dong, X. Wang, J. Li, Z. Lei, Z. Hu, J. Chen, H. Sun, H. Chen, X. Luo, X. Qian and Y. Yang, Rigid and Photostable Shortwave Infrared Dye Absorbing/Emitting beyond 1200 nm for High-Contrast Multiplexed Imaging, *J. Am. Chem. Soc.*, 2023, **145**, 12013–12022.

16 T. Z. Wang, Z. Y. Jiang and Z. P. Liu, 1,4-Bisvinylbenzene-Bridged BODIPY Dimers for Fluorescence Imaging in the Second Near-Infrared Window, *Org. Lett.*, 2023, **25**, 1638–1642.

17 L. Bai, P. Sun, Y. Liu, H. Zhang, W. Hu, W. Zhang, Z. Liu, Q. Fan, L. Li and W. Huang, Novel aza-BODIPY based small molecular NIR-II fluorophores for in vivo imaging, *Chem. Commun.*, 2019, **55**, 10920–10923.

18 B. Li, L. Lu, M. Zhao, Z. Lei and F. Zhang, An Efficient 1064 nm NIR-II Excitation Fluorescent Molecular Dye for Deep-Tissue High-Resolution Dynamic Bioimaging, *Angew. Chem., Int. Ed.*, 2018, **57**, 7483–7487.

19 X. Zhao, F. Zhang and Z. Lei, The pursuit of polymethine fluorophores with NIR-II emission and high brightness for in vivo applications, *Chem. Sci.*, 2022, **13**, 11280–11293.

20 S. S. Matikonda, D. A. Helmerich, M. Meub, G. Beliu, P. Kollmannsberger, A. Greer, M. Sauer and M. J. Schnermann, Defining the Basis of Cyanine Phototruncation Enables a New Approach to Single-Molecule Localization Microscopy, *ACS Cent. Sci.*, 2021, **7**, 1144–1155.

21 T. Chen, Y. Zheng, Y. Gao and H. Chen, Photostability investigation of a near-infrared-II heptamethine cyanine dye, *Bioorg. Chem.*, 2022, **126**, 105903.

22 R. Tapia Hernandez, M. C. Lee, A. K. Yadav and J. Chan, Repurposing Cyanine Photoinstability to Develop Near-Infrared Light-Activatable Nanogels for In Vivo Cargo Delivery, *J. Am. Chem. Soc.*, 2022, **144**, 18101–18108.

23 D. Möbius, Scheibe Aggregates, *Adv. Mater.*, 1995, **7**, 437–444.

24 E. E. Jelley, Spectral Absorption and Fluorescence of Dyes in the Molecular State, *Nature*, 1936, **138**, 1009–1010.

25 F. Wurthner, T. E. Kaiser and C. R. Saha-Moller, J-aggregates: from serendipitous discovery to supramolecular engineering of functional dye materials, *Angew. Chem., Int. Ed.*, 2011, **50**, 3376–3410.

26 X. Hu, C. Zhu, F. Sun, Z. Chen, J. Zou, X. Chen and Z. Yang, J-Aggregation Strategy toward Potentiated NIR-II Fluorescence Bioimaging of Molecular Fluorophores, *Adv. Mater.*, 2023, **36**, 2304848.

27 K. W. Lee, Y. Gao, W. C. Wei, J. H. Tan, Y. Wan, Z. Feng, Y. Zhang, Y. Liu, X. Zheng, C. Cao, H. Chen, P. Wang, S. Li, K. T. Wong and C. S. Lee, Anti-Quenching NIR-II J-Aggregates of Benzo[c]thiophene Fluorophore for Highly Efficient Bioimaging and Phototheranostics, *Adv. Mater.*, 2023, **35**, 2211632.

28 W. Chen, C. A. Cheng, E. D. Cosco, S. Ramakrishnan, J. G. P. Lingg, O. T. Bruns, J. I. Zink and E. M. Sletten, Shortwave Infrared Imaging with J-Aggregates Stabilized in Hollow Mesoporous Silica Nanoparticles, *J. Am. Chem. Soc.*, 2019, **141**, 12475–12480.

29 C. Sun, B. Li, M. Zhao, S. Wang, Z. Lei, L. Lu, H. Zhang, L. Feng, C. Dou, D. Yin, H. Xu, Y. Cheng and F. Zhang, J-Aggregates of Cyanine Dye for NIR-II in Vivo Dynamic Vascular Imaging beyond 1500 nm, *J. Am. Chem. Soc.*, 2019, **141**, 19221–19225.

30 C. Zhang, Y. Wu, F. Zeng, Y. Wen, J. Chen, G. Deng, L. Zhang, S. Zhao, S. Wu and Y. Zhao, Structurally Modulated Formation of Cyanine J-Aggregates with Sharp and Tunable Spectra for Multiplexed Optoacoustic and Fluorescence Bioimaging, *Angew. Chem., Int. Ed.*, 2024, **63**, e202406694.

31 K. Li, X. Duan, Z. Jiang, D. Ding, Y. Chen, G. Q. Zhang and Z. Liu, J-aggregates of meso-[2.2]paracyclophanyl-BODIPY dye for NIR-II imaging, *Nat. Commun.*, 2021, **12**, 2376.

32 Y. Zhu, P. Wu, S. Liu, J. Yang, F. Wu, W. Cao, Y. Yang, B. Zheng and H. Xiong, Electron-Withdrawing Substituents Allow Boosted NIR-II Fluorescence in J-Type Aggregates for Bioimaging and Information Encryption, *Angew. Chem., Int. Ed.*, 2023, **62**, e202313166.

33 X. Wang, Z. Jiang, Z. Liang, T. Wang, Y. Chen and Z. Liu, Discovery of BODIPY J-aggregates with absorption maxima beyond 1200 nm for biophotonics, *Sci. Adv.*, 2022, **8**, eadd5660.

34 X. Guo, J. Yang, M. Li, F. Zhang, W. Bu, H. Li, Q. Wu, D. Yin, L. Jiao and E. Hao, Unique Double Intramolecular and Intermolecular Exciton Coupling in Ethene-Bridged aza-BODIPY Dimers for High-Efficiency Near-Infrared Photothermal Conversion and Therapy, *Angew. Chem., Int. Ed.*, 2022, **61**, e202211081.

35 J. H. Kim, T. Schembri, D. Bialas, M. Stolte and F. Wurthner, Slip-Stacked J-Aggregate Materials for Organic Solar Cells and Photodetectors, *Adv. Mater.*, 2021, **34**, e2104678.

36 Z. Chen, A. Lohr, C. R. Saha-Moller and F. Wurthner, Self-assembled pi-stacks of functional dyes in solution: structural and thermodynamic features, *Chem. Soc. Rev.*, 2009, **38**, 564–584.

37 R. Misra and S. P. Bhattacharyya, *Intramolecular Charge Transfer: Theory and Applications*, Wiley-VCH, 1st edn, 2018.

38 H. Marciniak, N. Auerhammer, S. Ricker, A. Schmiedel, M. Holzapfel and C. Lambert, Reduction of the

Fluorescence Transition Dipole Moment by Excitation Localization in a Vibronically Coupled Squaraine Dimer, *J. Phys. Chem. C*, 2019, **123**, 3426–3432.

39 N. Q. Chako, Absorption of Light in Organic Compounds, *J. Chem. Phys.*, 1934, **2**, 644–653.

40 P. Jonkheijm, P. van der Schoot, A. P. Schenning and E. W. Meijer, Probing the solvent-assisted nucleation pathway in chemical self-assembly, *Science*, 2006, **313**, 80–83.

41 H. Yu, Y. Wang, Y. Chen and M. Ji, Rational design of a NIR-II fluorescent nanosystem with maximized fluorescence performance and applications, *Mater. Adv.*, 2021, **2**, 6058–6067.

42 J. A. Carr, D. Franke, J. R. Caram, C. F. Perkinson, M. Saif, V. Askoxylakis, M. Datta, D. Fukumura, R. K. Jain, M. G. Bawendi and O. T. Bruns, Shortwave infrared fluorescence imaging with the clinically approved near-infrared dye indocyanine green, *Proc. Natl. Acad. Sci. U. S. A.*, 2018, **115**, 4465–4470.

43 H. Mu, K. Miki, H. Harada, K. Tanaka, K. Nogita and K. Ohe, pH-Activatable Cyanine Dyes for Selective Tumor Imaging Using Near-Infrared Fluorescence and Photoacoustic Modalities, *ACS Sens.*, 2020, **6**, 123–129.

44 J. Li, J. Wang, L. Xu, H. Chi, X. Liang, J. Yoon and W. Lin, A Class of Activatable NIR-II Photoacoustic Dyes for High-Contrast Bioimaging, *Angew. Chem., Int. Ed.*, 2023, **63**, e20231263.

45 Y. Song, X. Tong, Y. Han and Q.-W. Zhang, Finely tunable NIR-II organic scaffolds for fluorescence/photoacoustic duplex imaging–guided noninvasive photothermal therapy of glioblastoma, *Aggregate*, 2025, **6**, e680.

46 S. Wang, X. Bi, H. Zhu, X. Ji, H. Lu and Z. Shen, Rational design of aggregation-induced emission-active bisboron complexes (BOQHYs) for high-fidelity lipid droplet imaging, *Aggregate*, 2025, **6**, e670.

47 Z. Jiang, X. Ma, K. Song, T. Wang, M. Dong, H. Liu, H. Gao, X. Wang, J. Zhao and Z. Liu, CCDC 2401346: Experimental Crystal Structure Determination, 2025, DOI: **10.5517/ccdc.csd.cc2llsss**; Z. Jiang, X. Ma, K. Song, T. Wang, M. Dong, H. Liu, H. Gao, X. Wang, J. Zhao and Z. Liu, CCDC 2401347: Experimental Crystal Structure Determination, 2025, DOI: **10.5517/ccdc.csd.cc2llstt**; Z. Jiang, X. Ma, K. Song, T. Wang, M. Dong, H. Liu, H. Gao, X. Wang, J. Zhao and Z. Liu, CCDC 2401348: Experimental Crystal Structure Determination, 2025, DOI: **10.5517/ccdc.csd.cc2llsvv**; Z. Jiang, X. Ma, K. Song, T. Wang, M. Dong, H. Liu, H. Gao, X. Wang, J. Zhao and Z. Liu, CCDC 2401349: Experimental Crystal Structure Determination, 2025, DOI: **10.5517/ccdc.csd.cc2llsww**.